Global and Planetary Change 257 (2026) 105259

Contents lists available at ScienceDirect

Global and Planetary Change

journal homepage: www.elsevier.com/locate/gloplacha

ENSO variations during the mid- to late Holocene: Evidence from coral growth rates spanning 2203 years in the northern South China Sea

Dahua Huang [a], Kefu Yu [a,b,*], Leilei Jiang [a], Wei Jiang [a]

[a] Guangxi Laboratory on the Study of Coral Reefs in the South China Sea, Coral Reef Research Center of China, School of Marine Sciences, Guangxi University, Nanning 530004, PR China
[b] Southern Marine Science and Engineering Guangdong Laboratory (Guangzhou), Guangzhou 511458, PR China

ARTICLE INFO

Editor: Dr. Fabienne Marret-Davies

Keywords:
Coral growth rate
Sea surface temperature
El Niño–Southern Oscillation
Mid- to late Holocene
Northern South China Sea

ABSTRACT

The El Niño–Southern Oscillation (ENSO) dominates global interannual climate variability and significantly impacts human societies. However, ENSO behavior during the Holocene remains poorly constrained and debated, limiting our ability to assess its long-term dynamics. Here, we present a 2203-year, discontinuous record of annual coral growth rates, derived from 113 U-series-dated fossil corals (*Porites lutea*) collected from eastern Hainan Island in the northern South China Sea (SCS), spanning 5829–2643 years before present (a BP, relative to 1950 Common Era [CE]). Using a robust calibration between coral growth rate and sea surface temperature (SST), we quantitatively reconstruct annual SST fluctuations in the northern SCS, ranging from 24.2 °C to 27.5 °C, with a mean of 25.6 ± 0.4 °C (1σ), approximately 0.7 °C lower than the baseline of 1982–2023 CE. The SST record reveals at least 18 cold periods occurring quasi-periodically at ~200-year intervals, with their durations shortening toward the Late Holocene. Since coral growth rates closely track local SST variability, interannual ENSO signals are reliably preserved in the coral archive. The inferred ENSO variability exhibits pronounced multidecadal modulation, transitioning from weaker-than-present, persistent La Niña-like conditions in the Mid-Holocene (~5800–4200 a BP) to stronger-than-present, prolonged El Niño-like conditions in the Late Holocene (~4200–2600 a BP). These ENSO shifts cannot be fully explained by external forcings such as orbital insolation or volcanic activity, highlighting the predominant role of internal ocean–atmosphere dynamics in modulating ENSO evolution during the Holocene.

1. Introduction

The El Niño–Southern Oscillation (ENSO) is the leading mode of interannual climate variability in the tropical Pacific and generates far-reaching hydroclimatic anomalies through coupled ocean–atmosphere teleconnections (Cai et al., 2020; Geng et al., 2023; McPhaden et al., 2006; Timmermann et al., 2018). During El Niño events, westerly wind anomalies generate downwelling Kelvin waves that deepen the eastern Pacific thermocline and warm the surface through the Bjerknes feedback, while the eastward shift of convection weakens the Walker circulation and induces drought across the western Pacific warm pool (Cai et al., 2021; Vialard et al., 2025). Conversely, La Niña events strengthen the trade winds and the zonal SST gradient, producing broadly opposite anomalies. ENSO is therefore a primary driver of global extremes, including droughts, floods, and heatwaves, and exerts substantial ecological and socioeconomic impacts (Cai et al., 2014; McPhaden, 2015). Although instrumental observations over the past ~150 years reveal pronounced decadal-scale ENSO fluctuations (Deser et al., 2010; Fedorov et al., 2020), major uncertainties remain regarding the influence of anthropogenic warming on ENSO variability (Lawman et al., 2022; Collins et al., 2010). Given that the instrumental record captures only a limited portion of ENSO's intrinsic variability, geological archives are essential for constraining its long-term behavior and improving climate model projections.

The Holocene (since 11,700 a BP, relative to 1950 Common Era [CE]) is particularly valuable as a climate analog for the present interglacial and provides an opportunity to investigate ENSO behavior under different background climate states. Coral-based reconstructions from the central and western tropical Pacific (Beck et al., 1997; Cobb et al., 2013; McGregor et al., 2013; Tudhope et al., 2001) suggest persistently weak ENSO variability during the Mid-Holocene, which is supported by marine sediment records from Peru (Rein et al., 2005). In contrast,

* Corresponding author at: School of Marine Sciences, Guangxi University, No. 100, Daxuedong Road, Xixiangtang District, Nanning 530004, Guangxi, China.
E-mail address: kefuyu@scsio.ac.cn (K. Yu).

https://doi.org/10.1016/j.gloplacha.2025.105259
Received 10 April 2025; Received in revised form 9 December 2025; Accepted 17 December 2025
Available online 18 December 2025

sediment records from Laguna Pallcacocha (Moy et al., 2002) and evidence from archaeological sites in Peru (Keefer et al., 1998) indicate episodes of strong ENSO variability during the Mid-Holocene. In addition, whether ENSO variability is primarily driven by natural external forcings (Adams et al., 2003; Grothe et al., 2019; Jiménez-Moreno et al., 2021) or internal climate system variability (Cobb et al., 2003; Dee et al., 2020; Wittenberg, 2009) remains vigorously contested. These discrepancies are often attributed to the limited temporal resolution of many paleoclimate records, highlighting the need for more high-resolution ENSO reconstructions.

Porites corals are highly sensitive to environmental changes and provide climatic information at a monthly to annual resolution, making them reliable proxies for reconstructing ENSO variability during the Holocene (Cobb et al., 2003; Corrége et al., 2000; Dee et al., 2020). The northern South China Sea (SCS) hosts widespread *Porites* corals that effectively capture ENSO signals (Dang et al., 2024; Jiang et al., 2023; Yu, 2012). However, diagenetic alteration of coral aragonite can compromise the fidelity of geochemical proxy records (Brachert et al., 2016). In contrast, coral growth rates, measured along the skeletal primary growth axis, are largely insensitive to post-depositional diagenesis

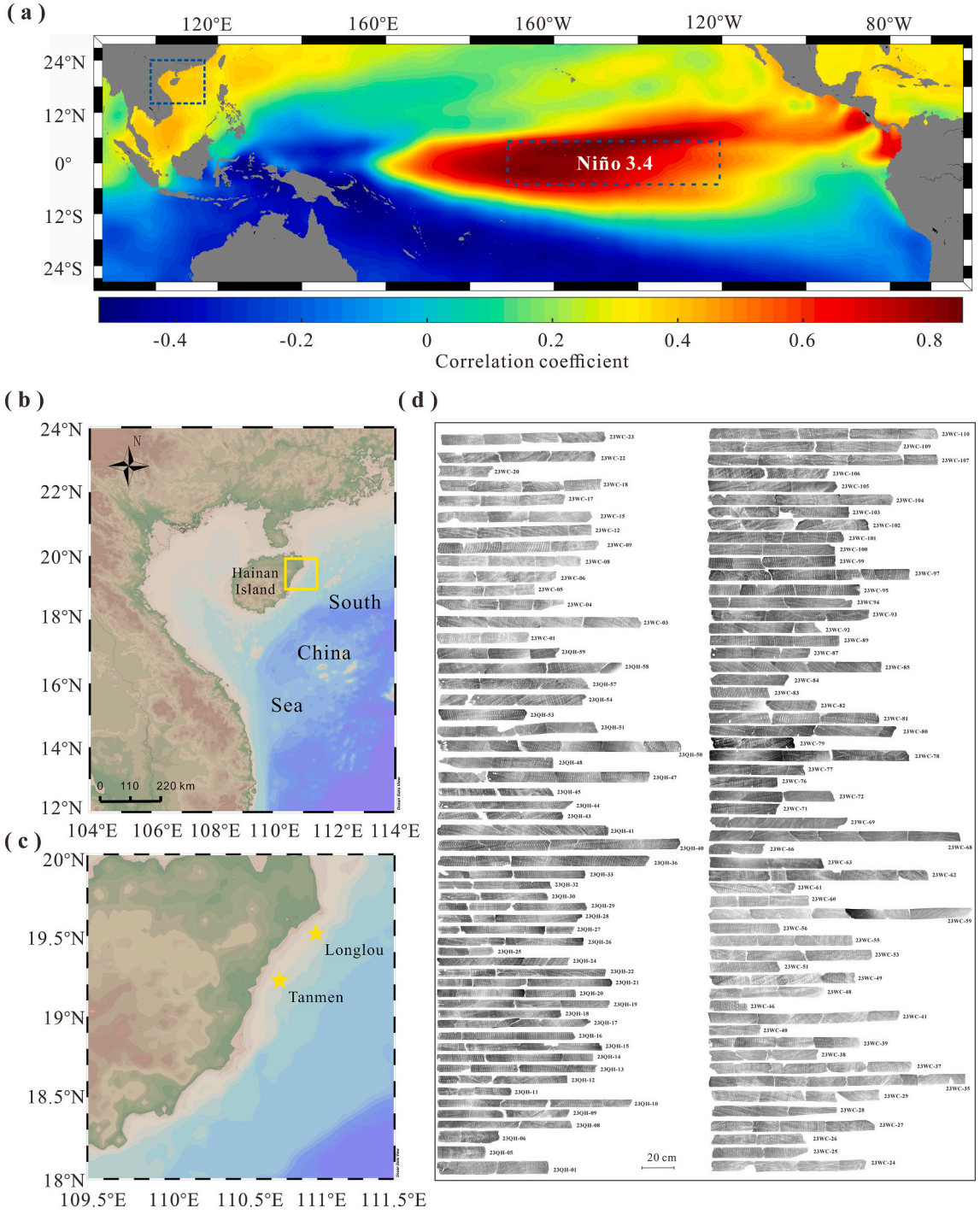

Fig. 1. Overview of the study area and fossil coral samples. (a) Spatial correlation between sea surface temperature (SST) in the Niño 3.4 region and SST in the study area (Jiang et al., 2021a). (b) Sampling locations. SST data are sourced from NOAA OISSTv2 (https://psl.noaa.gov/data/gridded/data.noaa.oisst.v2.html), and the map is generated using Ocean Data View program (https://odv.awi.de/). (c) X-ray images of the 113 fossil coral cores.

(Reuter et al., 2005), reducing this source of uncertainty. Consequently, analyzing *Porites* coral growth rates from the northern SCS offers a robust approach to improving the spatial and temporal resolution of ENSO reconstructions (Dang et al., 2020; Tao et al., 2024). Nonetheless, generating continuous multi-century coral records remains difficult due to the episodic preservation of corals and the discontinuous exposure of fossil colonies on uplifted reefs or reef flats (Cobb et al., 2013). As a result, most coral-based records are composite time series assembled from discrete samples, and truly long-term Holocene-scale continuous records remain scarce.

In this study, 113 fossil cores and one modern coral core (*Porites lutea*) collected from eastern Hainan Island in the northern SCS were analyzed. By integrating U-series dating of the fossils with annual growth-band counting from X-ray images, we constructed a discontinuous 2203-year record of annual coral growth rates, spanning approximately 5829 to 2643 a BP. Based on the relationship between modern coral growth rates and instrumental SST, a transfer function was developed to quantitatively reconstruct an annual SST record over this interval. Given that contemporary instrumental SST and coral growth rate–SST records effectively capture ENSO variability, this 2203-year-long record was used to assess long-term ENSO variability and its potential forcing mechanisms. The long-term, high-resolution SST series reconstructed from coral growth rates elucidates the dynamics of coral growth and ENSO variability over this interval, providing valuable insights into ENSO evolution and its driving mechanisms.

2. Study region

The SCS, located at the edge of the West Pacific Warm Pool, is influenced by the East Asian monsoon, with its interannual climate variability predominantly modulated by ENSO (Chen et al., 2023; Liu et al., 2016; Tan et al., 2016; Wang et al., 2023). Eastern Hainan Island (18°N–20°N, 110°E–111°E) is located in the northern SCS (Fig. 1a), where SST exhibits a distinct annual cycle, with higher SST from May to October (mean ~ 28.3 °C) and lower SST from January to March (~23.3 °C). The co-variability of SST between the northern SCS (including Hainan Island) and the Niño 3.4 region is attributed to the remote influence of ENSO activity through an "atmospheric bridge" (Klein et al., 1999). During El Niño events, weakening of the zonal SST gradient in the tropical Pacific enhances downward shortwave radiation and produces positive SST anomalies in the northern SCS (Jiang et al., 2021a, 2021b; Wang et al., 2000; Yan et al., 2011). Conversely, during La Niña events, negative SST anomalies are observed in the northern SCS as a result of a strengthened tropical Pacific gradient and reduced net solar radiation.

3. Materials and methods

3.1. Coral cores and dating

Coral samples (*Porites lutea*) were collected from eastern Hainan Island in 2023 CE (Fig. 1b–c). Coral cores were extracted from 113 dead colonies and one living colony using a hydraulic rig and a portable electric drill, with core diameters of 60 mm and 80 mm. The total lengths of the dead and living coral cores were approximately 111.9 m and 0.6 m, respectively. In the laboratory, each core was sliced into ~7 mm-thick sections. These sections were soaked in an 8 % H_2O_2 solution for 48 h to remove organic matter, then ultrasonically cleaned in deionized water for one hour to remove surface contaminants. Finally, after drying the sections in an oven at 37 °C, X-radiographs were obtained using a medical X-ray imaging system to identify annual growth-band patterns (Fig. 1d). Uranium-series dating of the dead coral cores was conducted using Multi-Collector Inductively Coupled Plasma Mass Spectrometer (MC-ICP-MS) at the University of Queensland, Australia, following the analytical methods detailed in Yu et al. (2006) and Zhao et al. (2009).

3.2. Growth rate measurement

Coral growth rate was quantified by measuring the distances between annual density bands visible in the X-ray images (Cooper et al., 2012; Helmle et al., 2011; Saenger et al., 2009; Tao et al., 2024). The RadiAnt DICOM Viewer software was used to convert the original X-ray negatives into positive grayscale images for analysis. Measurements were taken along the primary growth axis of each coral (DeLong et al., 2013), by measuring the distance between the midpoints of successive high-density bands, with each adjacent black–white band pair representing one year of skeletal extension. The mean of multiple measurements was calculated as the annual growth rate for that year. Annual growth-band counts derived from X-ray images were then integrated with Uranium-series dating results to establish the chronological framework, assigning each measured coral growth layer to a specific calendar year within dating uncertainties.

3.3. Data acquisition and processing

To evaluate the degree to which SST variability in the northern SCS reliably reflects ENSO variability, monthly SST data (1982–2023 CE) for eastern Hainan Island (18°N–20°N, 110°E–111°E) and for the Niño 3.4 region (5°S–5°N, 170°W–120°W) were compiled from the NOAA Optimum Interpolation SST Analysis dataset (OISSTv2, https://psl.noaa.gov/data/gridded/data.noaa.oisst.v2.html). Sea surface salinity (SSS) data were obtained from the UK Met Office EN4 dataset (https://www.metoffice.gov.uk/hadobs/en4/), and outgoing longwave radiation (OLR) data were extracted from the NOAA HIRS L1B product (Lee et al., 2007). These environmental parameters were used to assess their relative influence on coral growth and to quantify the extent to which SST is the dominant driver in the northern SCS.

Linear regression, spectral analysis, and wavelet transforms were conducted using PAST software. Linear interpolation was performed in SPSS software to facilitate comparison among datasets. In addition, SST anomalies (SSTA) were calculated as deviations from the climatology of the corresponding timescale for each SST record. The SST anomaly series was processed with a 3–7-year band-pass filter to isolate ENSO-frequency variability (Jiang et al., 2021a), and its total variance was taken as an indicator of ENSO intensity (Cobb et al., 2003; Comboul et al., 2015; Jiang et al., 2023). Furthermore, a 30-year sliding window was applied to calculate relative variance (Cobb et al., 2013; Dang et al., 2020), allowing ENSO intensity to be evaluated relative to 1994–2023 CE. In addition, probability density functions (PDFs) based on kernel density estimation were employed to characterize the temporal distribution of ENSO variance (Lawman et al., 2020).

The empirical calibration threshold method (Hereid et al., 2013) was applied to assess detection of ENSO events. Specifically, an initial threshold of 0.01 °C was incrementally adjusted by 0.01 °C to optimize detection of ENSO events (Jiang et al., 2021a; Tao et al., 2024). Based on the optimized thresholds, El Niño events were defined as SST anomalies exceeding 0.12 °C and La Niña events as those falling below −0.12 °C. Furthermore, the detection capability of the SST record from Hainan Island was quantified as the proportion of ENSO events correctly identified from the filtered SSTA series.

4. Results

4.1. Chronology construction

The modern coral core (24NH45) from Hainan Island spans 1982–2023 CE. The U and Th isotopic compositions and corresponding U-Th ages of the 113 fossil corals are listed in Table S1 (errors at 2σ). An age model for each coral was constructed by integrating U-Th ages with annual growth-band patterns identified in X-ray images. Across the 111.9 m of fossil cores and their associated X-ray images, a total of 7085 annual growth layers were identified. Individual fossil cores record

15–164 years of growth, with a mean length of ~63 years (Table S2).

Based on the established chronology, 1608 years of overlap were identified among the fossil corals (Fig. S1c), forming six continuous segments that together span 2203 years of the Mid- to Late Holocene. These segments (ages relative to 1950 CE) are 5829–5780 a BP (50 years), 5733–5149 a BP (585 years), 4667–4470 a BP (198 years), 4403–3212 a BP (1192 years), 3008–2939 a BP (70 years), and 2750–2643 a BP (108 years). The U-Th age uncertainties for each segment are reported at 2σ (Table S1). These discontinuous but temporally extensive segments constitute the high-resolution coral archive used in this study and substantially expand existing tropical coral records.

4.2. Characteristics of coral growth rate

The modern coral (1982–2023 CE) exhibits a mean annual growth rate of 1.246 ± 0.148 (1σ) cm/a, with a maximum of 1.700 cm/a, a minimum of 0.925 cm/a, and an overall amplitude of 0.775 cm/a. In comparison, the 113 fossil corals show a mean growth rate of 1.031 ± 0.138 (1σ) cm/a, with a maximum of 1.620 cm/a, a minimum of 0.584 cm/a, and an amplitude of 1.036 cm/a (Fig. S1a). On average, the fossil corals grew approximately 0.215 cm/a more slowly than the modern coral yet displayed substantially greater variability in annual growth rates.

Since the overlapping coral segments displayed broadly consistent trends, growth rates within the overlapping intervals were averaged to generate six composite continuous segments (Fig. S1b): (1) 5829–5780 a BP (50 years, mean 0.746 cm/a): growth rates declined from ~0.881 cm/a to 0.652 cm/a. (2) 5733–5149 a BP (585 years, 1.010 cm/a): growth rates exhibited an overall increasing trend, ranging from 0.653 cm/a to 1.385 cm/a, with minima occurring at ~5440 a BP (0.848 cm/a) and ~ 5250 a BP (0.821 cm/a). (3) 4667–4470 a BP (198 years, 1.058 cm/a): growth rates decreased sharply from 1.480 cm/a to 0.584 cm/a, yielding an amplitude of ~0.9 cm/a. (4) 4403–3212 a BP (1192 years, 1.034 cm/a): growth rates showed an overall decreasing trend with internal fluctuations. Notably low values occurred at ~4200 a BP (0.603 cm/a), ~4000 a BP (0.881 cm/a), ~3800 a BP (0.926 cm/a), ~3600 a BP (0.671 cm/a), ~3400 a BP (0.760 cm/a) and ~ 3200 a BP (0.754 cm/a), recurring at intervals of approximately 200 years. (5) 3008–2939 a BP (70 years, 0.940 cm/a): growth rates increased rapidly from 0.622 cm/a to 1.380 cm/a. (6) 2750–2643 a BP (108 years, 1.106 cm/a): growth rates rose from 0.818 cm/a to 1.450 cm/a (~2675 a BP) and subsequently declined to 0.707 cm/a.

Overall, the coral growth record can be divided into three broad phases: a period of increasing growth rates (~5800–4400 a BP), followed by a period of decreasing growth rates (~4400–4200 a BP), and a final period characterized by oscillatory growth-rate variability (~4200–2600 a BP). These patterns reflect the high sensitivity of coral growth to environmental variation and provide high-resolution insights into the climate dynamics during the Mid- to Late Holocene.

5. Discussion

5.1. Modern Calibration: coral growth rates as proxies for SST and ENSO

5.1.1. Coral growth rate thermometer

The primary environmental factors controlling coral skeletal growth include SST, SSS, and light availability (Cooper et al., 2012; Lough and Barnes, 1997). To assess their relative influence in the northern SCS, regression analyses were performed between coral growth rates and instrumental records of SST, SSS, and OLR (Fig. S2). The resulting coefficients of determination (R^2) are 0.836 for SST, but only 0.001 for SSS and 0.003 for OLR, indicating that SST is by far the dominant driver of coral growth-rate variability in this region. This interpretation is consistent with findings from Hainan Island (Nie et al., 1997) and the Xisha Islands (Tao et al., 2024), which similarly identified SST as the primary control on coral growth. A strong positive correlation ($r = 0.91$, $P < 0.0001$, $n = 42$) was observed between instrumental SST and coral growth rates from 1982 to 2023 CE in eastern Hainan Island (Fig. 2a). Based on this relationship, a coral growth rate–SST conversion equation (Fig. 2b) was developed using Reduced Major Axis (RMA) regression (Solow and Huppert, 2004):

$$\mathrm{SST}\ (^{\circ}\mathrm{C}) = 3.172\ (\pm 0.200) \times \mathrm{L}\ (\mathrm{cm}) + 22.356\ (\pm 0.251)\ (1\sigma) \quad (1)$$

$$R^2 = 0.84, n = 42, p < 0.0001.$$

where L denotes coral growth rate. From Eq. (1), an increase of 1 mm in coral growth rate corresponds to an increase of 0.3 ± 0.02 °C in SST. Using this calibration, the SST history for eastern Hainan Island from 1982 to 2023 CE was quantitatively reconstructed. The coral-derived SST values range from ~25.3 to 27.8 °C with a mean of 26.3 ± 0.4 °C (1σ), in excellent agreement with the instrumental SST range of 25.3–27.4 °C (26.3 ± 0.4 °C; Fig. S3a) over the same interval.

Over 1982–2023 CE, the coral-based SST closely tracks the instrumental SST in eastern Hainan Island (Fig. S3a), confirming that coral growth rates faithfully capture contemporary temperature variability. The two records exhibit consistent dominant periodicities in their spectral power (Fig. 2c-d), and the 2.5–97.5th percentile ranges of their probability density distributions almost entirely overlap (coral: −2.2 to 1.7, instrumental: −2.0 to 1.9; Fig. S3b), further demonstrating their strong similarity. Together, these results indicate that coral growth rates effectively capture contemporary SST variability in this region. These findings are consistent with observations from other regions, including the Great Barrier Reef (Cooper et al., 2008; Lough and Barnes, 1997), the southwestern Indian Ocean (Cooper et al., 2012), and the Caribbean Sea (Kwiatkowski et al., 2013; Saenger et al., 2009), where positive correlations between coral growth rates and SST have been documented. Notably, Lough and Barnes (2000) reconstructed twentieth-century SST in the Great Barrier Reef and reported that a 1 °C increase in SST corresponded to a 3 mm/year increase in coral growth rates. Such parallels provide further confidence that coral growth rate serves as a reliable "thermometer" proxy for past SST.

5.1.2. Modern ENSO variability

The modern instrumental and coral-derived SST records from Hainan Island both exhibit dominant interannual cycles of 2.3 years (Fig. 2c) and 2.2 years (Fig. 2d), respectively, consistent with the typical ENSO cycle. Furthermore, regression analyses between band-pass-filtered instrumental SST anomalies (detrended relative to the mean of 1982–2023 CE) in Hainan Island and those in the Niño 3.4 region, as well as between coral-derived SSTA from Hainan Island and instrumental SSTA in the Niño 3.4 region, yield statistically significant correlations ($r = 0.55$, $p < 0.001$, Fig. S4a; and $r = 0.31$, $p < 0.05$, Fig. 3c, respectively). In addition, the probability distribution of the coral-recorded SSTA closely matches that of the instrumental Niño 3.4 SSTA, exhibiting comparable 2.5–97.5 % ranges (coral-based: −2.2 to 1.7, Niño 3.4: −2.1 to 1.7; Fig. 3d). We further compared the coral growth rate record from Hainan Island to the coral $\delta^{18}O$ anomaly record from Fanning Island in the central tropical Pacific, which serves as a robust proxy for ENSO variability (Cobb et al., 2013). The two records exhibit a strong negative correlation ($r = -0.71$, $p < 0.001$, $n = 23$), and their probability density distributions show close agreement (Fig. 3a–b). In summary, these results demonstrate that SSTs in eastern Hainan Island are significantly modulated by ENSO variability. Because coral growth rates closely track local SST fluctuations, they enable robust reconstruction of ENSO-related climate variability.

To explicitly identify ENSO events, a 3–7-year band-pass filter and a standard event-threshold analysis were applied (Dang et al., 2024; Hereid et al., 2013; Jiang et al., 2021a), using a 30-year sliding window anchored to the period of 1994–2023 CE. Based on the threshold criterion, the annual SST records from the Niño 3.4 region correctly identify

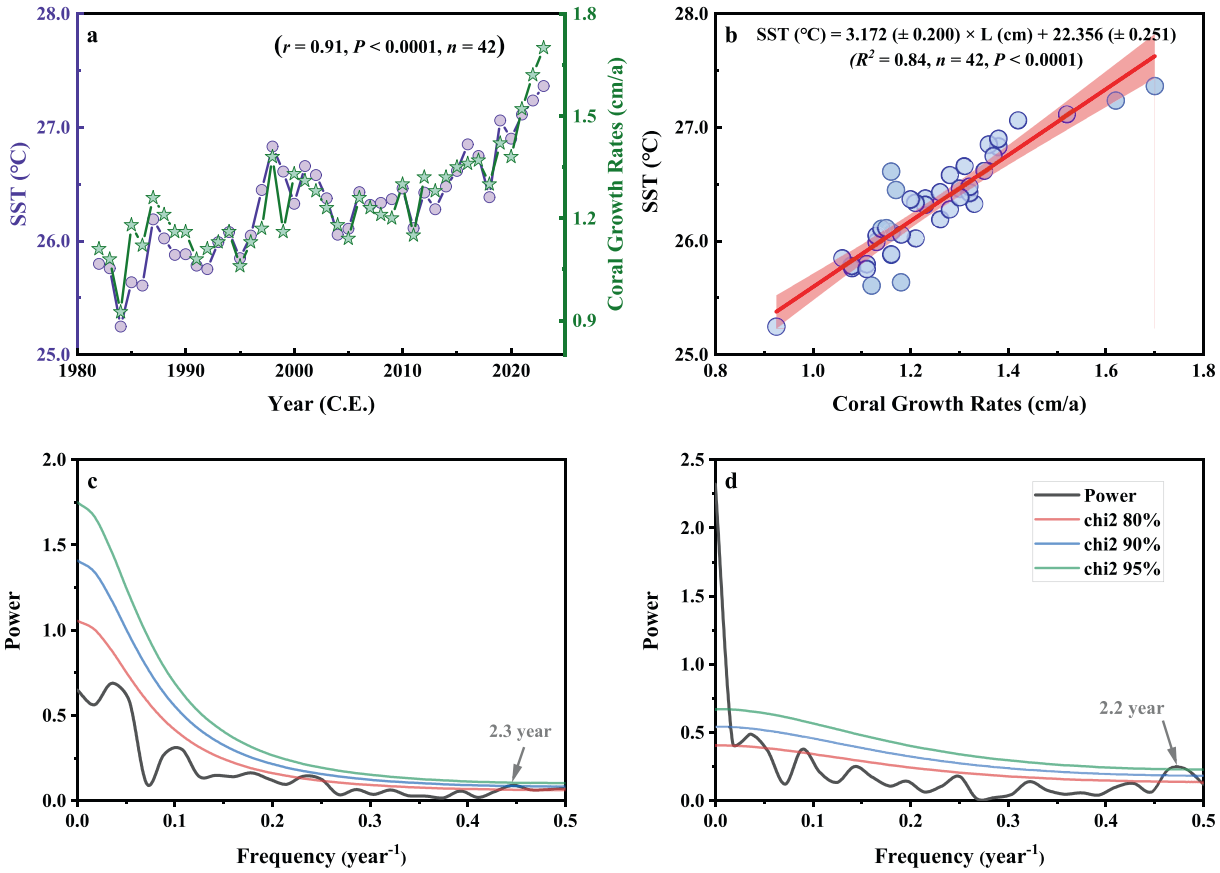

Fig. 2. Establishment of the coral growth rate–sea surface temperature (SST) conversion equation and spectral characteristics of SST variability in Hainan Island. (a) Comparison and (b) regression analysis of the relationship between coral growth rate and SST in the northern South China Sea. (c) Spectral analysis of instrumental SST (1982–2023 CE) and (d) coral growth rate–derived SST (1982–2023 CE). The green, blue, and red lines denote the 80 %, 90 %, and 95 % confidence levels, respectively. (For interpretation of the references to colour in this figure legend, the reader is referred to the web version of this article.)

7 El Niño events (missing 2) and 6 La Niña events (Fig. S4b). This corresponds to a detection rate of 78 % (7/9) for El Niño events and full detection (6/6) of La Niña events over 1994–2023 CE. The two missed El Niño events (1994 and 2004 CE) were likely weak in amplitude, and the conversion from monthly to annual resolution may have smoothed out these weaker ENSO signals. The instrumental SST record from Hainan Island correctly identified 7 El Niño events (missing 2) and 5 La Niña events (with 1 false alarm and 1 missed), achieving a detection rate of 78 % (7/9) for El Niño events and 83 % (5/6) for La Niña events (Fig. S4c). Similarly, our coral record from Hainan Island accurately captured 7 El Niño events (missing 2) and 4 La Niña events (with 1 false alarm and 2 missed), corresponding to a detection rate of 78 % (7/9) for El Niño events and 67 % (4/6) for La Niña events over 1994–2023 CE (Fig. 3e). Notably, both instrumental and coral records reveal an increasing trend in ENSO variance during 1982–2023 CE (Fig. S4d; Fig. 3f). Therefore, these results demonstrate that coral growth rates from Hainan Island reliably record ENSO variability at interannual timescales. Similar ENSO detectability based on growth rate has been documented for modern *Porites* coral from the Xisha Islands (Tao et al., 2024), further supporting the robustness of coral growth rate as an ENSO-sensitive proxy.

5.2. Fossil coral insights into SST fluctuation and ENSO variability

5.2.1. Reconstruction of SST changes during the mid- to late Holocene

Using the established calibration equation, SST variations in the northern SCS were quantitatively reconstructed during 5829–2643 a BP (Fig. 4a). The six continuous coral-derived segments (Table 1) indicate SST ranges of 24.4–25.2 °C (5829–5780 a BP), 24.4–26.8 °C (5733–5149 a BP), 24.2–27.1 °C (4667–4470 a BP), 24.3–27.2 °C (4403–3212 a BP), 24.3–26.7 °C (3008–2939 a BP), and 24.6–27.0 °C (2750–2643 a BP). The full 2203-year composite record yields a mean SST of 25.6 ± 0.4 °C, approximately 0.7 °C lower than the modern baseline (26.3 ± 0.4 °C, 1982–2023 CE). These results indicate that the Mid- to Late Holocene climate in the northern SCS was, on average, cooler than at present, consistent with previous coral-based reconstructions and marine sediment records from the northern SCS (Chen et al., 2024, Fig. 4h; Yang et al., 2019, Fig. 4d). Collectively, our coral record offers robust constraints on the timing and amplitude of oscillatory temperature variations during the Mid- to Late Holocene in this region.

Despite the overall cooling trend, at least 14 distinct warm episodes, with SSTs either comparable to or exceeding modern levels, can be identified within this 2203-year record (Fig. S5, Table S3). Several of these warming events coincide with well-documented periods of coral thermal stress and bleaching (Wang et al., 2021, Fig. 4f; Xu et al., 2017), including those occurring at ~5300 a BP, ~4568 a BP, ~3900 a BP, and ~ 3654 a BP. This pattern is further supported by coral records from Leizhou Peninsula (Yu et al., 2005, Fig. 4h), which report SSTs ~0.5 °C higher than in the 1990s around 4961 ± 54 a BP. These correlations suggest that modern-like or warmer SSTs have been reached repeatedly during the Mid- to Late Holocene, with deleterious impacts on reef ecosystems.

Using 25.2 °C (the annual minimum during 1982–2023 CE) as a threshold, at least 18 cold periods on an interannual scale are identified (Fig. S6–7; Table S4), with 5 pronounced multidecadal cold intervals using a 30-year sliding average (Fig. S6). The most severe cold interval occurred between 5829 and 5780 a BP (24.7 °C), representing a cooling of 1.6 °C relative to 1982–2023 CE. These prolonged cooling phases are

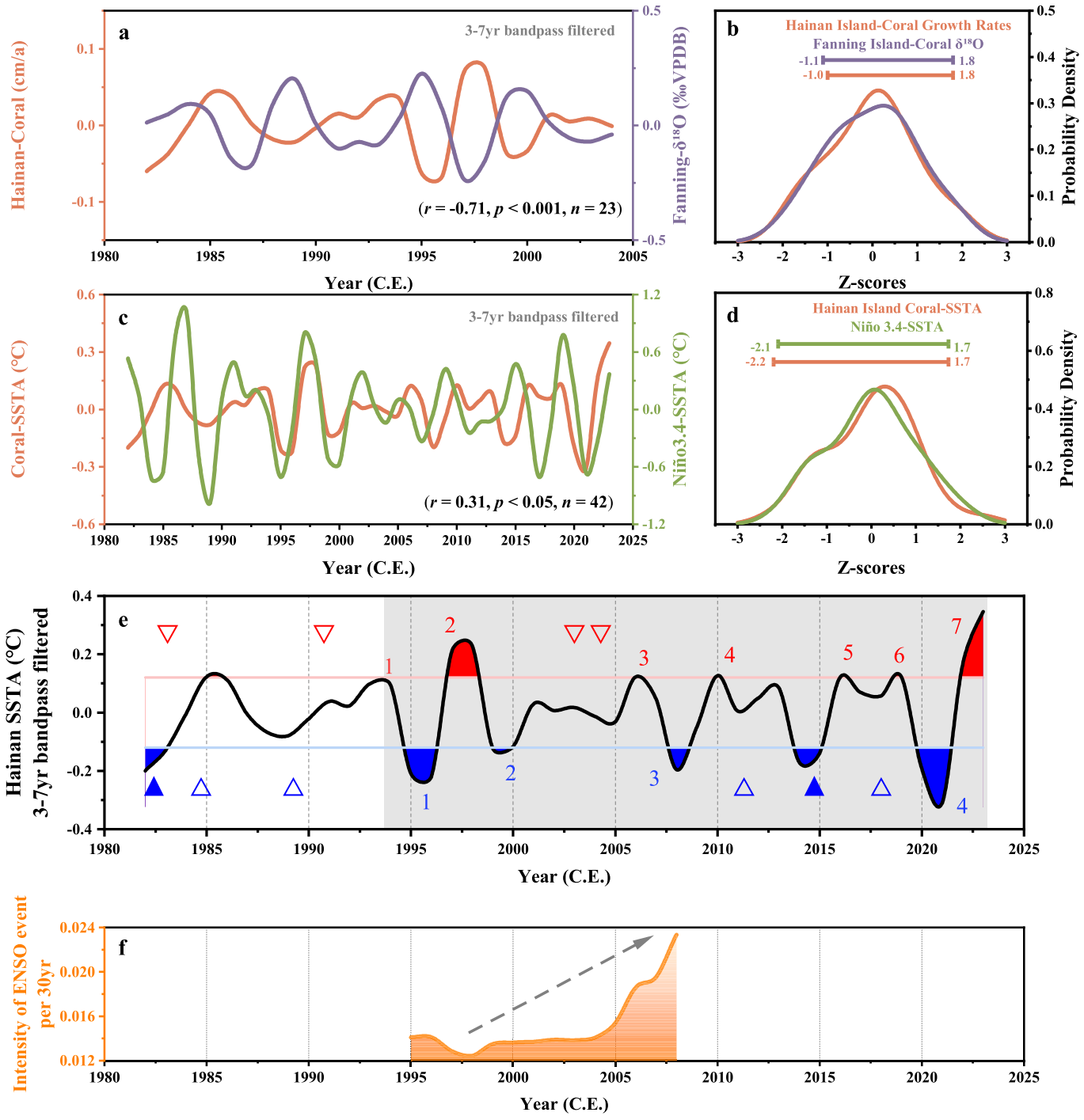

Fig. 3. El Niño–Southern Oscillation (ENSO) signals and variability inferred from modern coral records. (a) Filtered sea surface temperature anomalies (SSTA) and (b) probability density functions (PDFs) of coral records from Hainan Island (orange) and Fanning Island (purple; Cobb et al., 2013) during their overlapping interval (1982–2004 CE). (c) Relationship and (d) PDFs of 3–7-year band-pass-filtered SSTA from Hainan Island (orange) and the Niño 3.4 region (green) over their overlapping period (1982–2023 CE). (e) Extraction of ENSO events from coral-based SSTA using the defined threshold. Red and blue shading indicate identified El Niño and La Niña events, respectively; open triangles denote false negatives, and solid triangles denote false positives. The interval of 1994–2023 CE is highlighted by gray shading. (f) ENSO intensity derived from the variance of the extracted ENSO signal using a 30-year sliding window (1982–2023 CE). Horizontal bars in panels (b) and (d) indicate the 2.5–97.5 percentile ranges. All records in panels (b) and (d) are standardized using *Z*-scores for comparison. El Niño events are defined as SSTA exceeding 0.12 °C and La Niña events as SSTA below −0.12 °C. (For interpretation of the references to colour in this figure legend, the reader is referred to the web version of this article.)

not isolated features but are consistent with widespread paleoclimate evidence from the northern SCS and adjacent regions. Coral Sr/Ca records from Hainan Island indicate a rapid SST decline during the 4200 a BP event (Chen et al., 2023, 2024, Fig. 4h). Coral growth-rate archives from the Xisha Islands (Dang et al., 2020, Fig. 4h; Zhang et al., 2014, Fig. 4h) document SST reductions of 1.0 °C (4420–4312 a BP), 1.3 °C (4189–4112 a BP), and 0.9 °C (2985–2904 a BP) relative to 1887–2007 CE. Similarly, coral records from the Great Barrier Reef (Sadler et al., 2016, Fig. 4g), the central tropical Pacific and western Pacific (Bova et al., 2021, Fig. 4c; Rodriguez et al., 2019, Fig. 4g; Stott et al., 2004,

Fig. 4b), and Indonesia (Abram et al., 2009, Fig. 4g) indicate cooling events centered around 5800 a BP, ~5200 a BP, ~4400 a BP, ~4200 a BP, and ~ 3200 a BP, all of which correspond closely to cold intervals detected in our coral-derived SST record.

Significantly, these coral-based cold intervals exhibit a recurring periodicity of ~200 years. This cycle is consistent with independent Holocene climate reconstructions. For example, the global temperature stack compiled by (Marcott et al., 2013, Fig. 4e) documents cooling events at broadly similar ~200-year intervals. Additional support is provided by solar irradiance reconstructions, which highlight the de Vries (~208-year) solar cycle as a persistent feature of centennial-scale solar variability (Steinhilber et al., 2009, Fig. S8d). The recurrence of

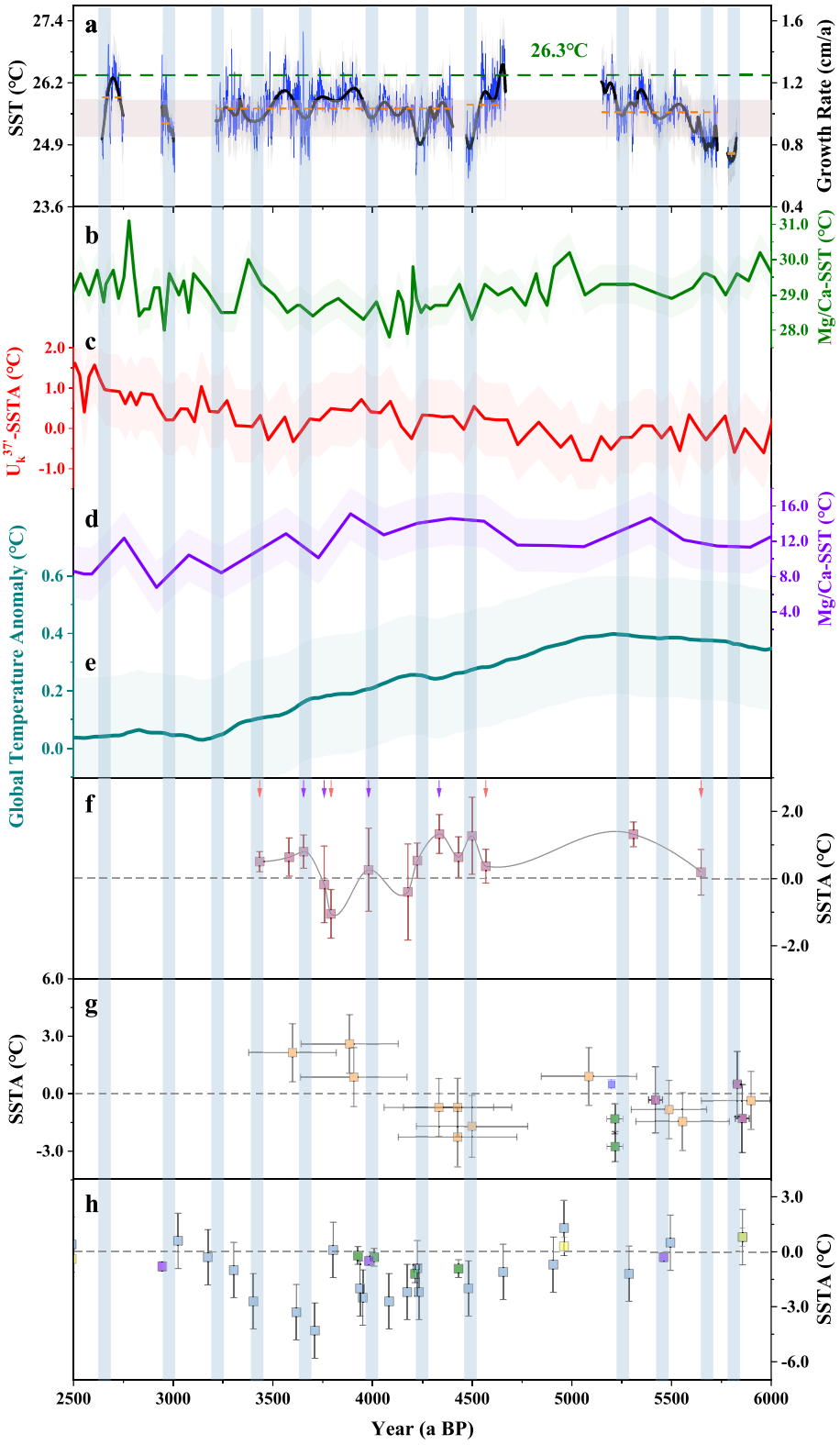

(caption on next page)

Fig. 4. Growth rate–derived sea surface temperature (SST) reconstruction from fossil corals in Hainan Island compared with regional and global proxy records. (a) Reconstructed SST variability from this study. The gray shading represents the ±1σ uncertainty range; the orange dashed line denotes the mean SST of the six continuous segments (5829–5780 a BP, 5733–5149 a BP, 4667–4470 a BP, 4403–3212 a BP, 3008–2939 a BP, and 2750–2643 a BP); the red shaded band indicates the range of mean annual SST values across all fossil coral reconstructions; the green dashed line marks the instrumental mean SST for 1982–2023 CE; and the black curve shows the 30-year sliding mean. (b) SST reconstruction based on Mg/Ca of planktonic foraminifera from the western Pacific (Stott et al., 2004). (c) Alkenone-based, UK'_{37} SST reconstruction from the western Pacific (Bova et al., 2021). (d) SST reconstruction based on Mg/Ca of planktonic foraminifera from the northern South China Sea (Yang et al., 2019). (e) Holocene global temperature compilation sequence (Marcott et al., 2013). (f) Coral Sr/Ca-based SST anomaly reconstruction from the northern SCS (Wang et al., 2021). Arrows denote coral bleaching events: red arrows mark samples containing a single mortality surface, whereas purple arrows indicate samples exhibiting both mortality surfaces and growth discontinuities. (g) Coral-based SST anomaly reconstructions from the Mentawai Islands (Abram et al., 2009, orange squares), Muschu/Koil Island (Abram et al., 2009, purple squares), the Great Barrier Reef (Sadler et al., 2016, green squares), and the central tropical Pacific (Rodriguez et al., 2019, blue squares). (h) Coral Sr/Ca- and growth rate–based SST anomaly reconstructions from the northern SCS (Chen et al., 2024, blue squares; Dang et al., 2020, green squares; Yu et al., 2005, yellow squares; Zhang et al., 2014, purple squares). (For interpretation of the references to colour in this figure legend, the reader is referred to the web version of this article.)

Table 1
Distributional periods of fossil corals and the range of their growth rates and SST variations.

Distribution period ± 2σ (a BP)	Period duration (year)	Range of growth rates (cm/a)	Average growth rate (cm/a)	Range of SST (°C)	Average SST (°C)	SST Polarization (°C)
5829–5780	50	0.652–0.881	0.746	24.4–25.2	24.7 ± 0.4	0.8
5733–5149	585	0.653–1.385	1.010	24.4–26.8	25.6 ± 0.4	2.4
4667–4470	198	0.584–1.480	1.058	24.2–27.1	25.7 ± 0.4	2.9
4403–3212	1192	0.603–1.530	1.034	24.3–27.2	25.6 ± 0.4	2.9
3008–2939	70	0.622–1.380	0.940	24.3–26.7	25.3 ± 0.4	2.4
2750–2643	108	0.707–1.450	1.106	24.6–27.0	25.9 ± 0.4	2.4

~200-year cold intervals in our fossil coral record may therefore reflect sensitivity to these cyclic variations in solar output, superimposed on regional ocean–atmosphere feedbacks in the tropical Pacific.

However, solar forcing is unlikely to have acted as the sole driver of these cooling phases. The timing and magnitude of several SST anomalies do not align precisely with known solar minima, indicating that internal climate processes modulated their regional expression. ENSO-related ocean–atmosphere dynamics likely amplified or dampened the external solar signal, while the East Asian monsoon system, tightly coupled with tropical western Pacific SST, may have further reinforced these cooling intervals. The reconstructed SST minima coincide with reduced East Asian Summer Monsoon intensity inferred from cave speleothems and lacustrine records (Wang et al., 2005, Fig. S8c; Yancheva et al., 2007, Fig. S8b), suggesting that these cold phases formed part of broader shifts in the East Asian–western Pacific climate system.

In summary, the coral-derived cold events in the northern SCS are consistent with regional and global evidence for Holocene cooling. Their quasi-200-year recurrence pattern points to a potential solar pacing, yet the amplitude and timing of the cooling intervals also highlight the role of internal ocean–atmosphere variability and monsoon-ENSO interactions. These findings underscore the need to integrate coral archives with broader multi-proxy datasets to better constrain the mechanisms governing Holocene tropical climate variability.

5.2.2. Reconstruction of ENSO variability during the mid- to late Holocene

The coral-derived SST record during 5829–2643 a BP exhibits pronounced 2–7-year cycles (Fig. S9), consistent with canonical ENSO variability, but with dominant cycles that differ from those of the modern reference period (1982–2023 CE; Fig. 2c–d). High-frequency interannual ENSO signals (Fig. S10) are also identified during 5733–5149 a BP, 4667–4470 a BP, and 4403–3212 a BP. Together, these features indicate that ENSO variability during the Mid- to Late Holocene was neither stationary nor uniform, but instead characterized by notable changes in both frequency and amplitude. The distribution estimated from fossil-based SST anomalies (2.5–97.5 percentile range; Fig. S11) also departs from those of modern coral records (Fig. 3d), further reflecting the instability of ENSO behavior. Moreover, the probability distributions of three fossil coral segments (5829–5780 a BP, 3008–2939 a BP, and 2750–2643 a BP) are skewed toward positive anomalies, suggesting El Niño-like background states, whereas the interval of 5733–5149 a BP is skewed toward negative anomalies, indicating a potential association with La Niña-like conditions.

A 3–7-year band-pass filter was applied to isolate ENSO signals (Fig. 5a) in the coral-derived SST anomalies, and a 30-year moving window was used to reveal interdecadal fluctuations in SSTA from the northern SCS (Fig. 5c). The same 30-year window was employed to count El Niño events and La Niña events, thereby tracking interdecadal trends in ENSO event frequency (Fig. 5d). ENSO intensity was assessed by calculating the variance of the filtered SSTA within a 30-year sliding window (Fig. 5b), using the period of 1994–2023 CE (variance is 0.0233) as the modern reference. Based on these metrics, 15 periods of weak ENSO variability and 16 periods of strong ENSO variability were identified during the Mid- to Late Holocene (Fig. S12, Table 2). These results demonstrate that the Mid-Holocene was not a period of uniformly suppressed ENSO activity, but rather characterized by alternating phases of weak and strong ENSO expression. Notably, the marked increase in strong ENSO intervals after the 4.2 ka event suggests that ENSO variability intensified during the Late Holocene.

Multiple independent proxy records corroborate the evolutionary pattern of ENSO variability inferred from our coral data. For instance, marine radiocarbon reservoir age reconstructions from the northern SCS (Yu et al., 2010) indicate weakened ENSO variability around 5800–5600 a BP, consistent with the low ENSO variance identified for this interval. Coral records from New Caledonia (Lazareth et al., 2013) provide evidence for increased El Niño occurrence around 5500–5100 a BP, in agreement with speleothem $\delta^{18}O$ records that suggest wetter tropical conditions during this period (Tian et al., 2023, Fig. 6c), as well as the heightened El Niño activity reconstructed in our study. In contrast, coral fluorescence data from the Great Barrier Reef (Leonard et al., 2016) indicate reduced ENSO variability during 5200–4300 a BP, a trend reflected in eastern Hainan Island and central equatorial Pacific coral $\delta^{18}O$ records (McGregor et al., 2013; Sun et al., 2005), titanium concentrations in Cariaco Basin sediments (Haug et al., 2001, Fig. 6e), and our coral-derived variance.

Notably, during the 4.2 ka event, coral growth rates and Sr/Ca from the northern SCS (Dang et al., 2020, 2024) document a two-stage ENSO response in which variance decreased to 27 % of the modern level in the early phase and subsequently recovered to 63 % of the modern level in the late phase. This pattern matches the transient ENSO weakening followed by recovery observed in our reconstruction for this climate perturbation. After ~4200 a BP, ENSO variance exhibits a strengthening trajectory, supported by Tridacna records from the SCS that indicate

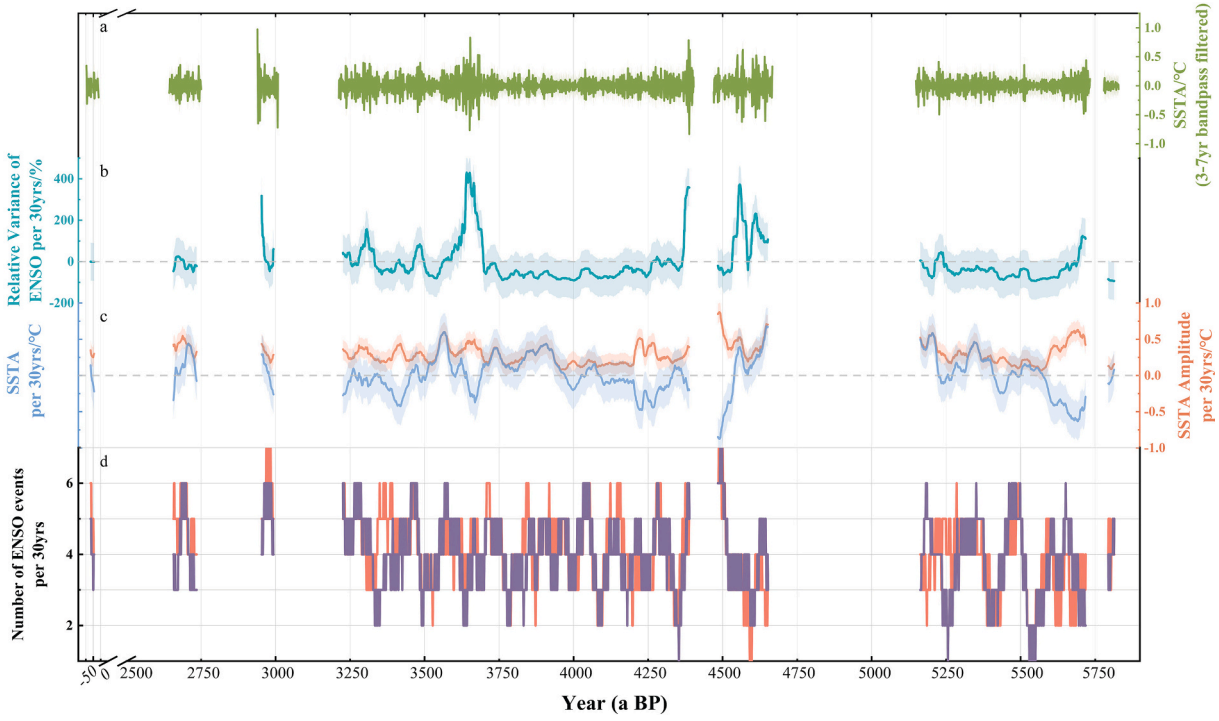

Fig. 5. El Niño–Southern Oscillation (ENSO) variability and sea surface temperature anomaly (SSTA) fluctuations inferred from fossil coral records in the northern South China Sea. (a) ENSO signals extracted from the coral-derived SSTA series using a 3–7-year band-pass filter. (b) ENSO intensity quantified as the variance of the filtered SSTA within a 30-year sliding window, expressed relative to the baseline of 1994–2023 CE. (c) Interdecadal variations in SSTA revealed by applying a 30-year sliding mean, where the blue curve represents the long-term trend and the orange curve denotes the corresponding amplitude changes. (d) Interdecadal ENSO frequency derived from a 30-year sliding window, with red and blue curves indicating the number of El Niño and La Niña events per 30-year window, respectively. (For interpretation of the references to colour in this figure legend, the reader is referred to the web version of this article.)

increasing ENSO variability during 4000–3000 a BP (Zhou et al., 2022). By ~3000 a BP, multiple proxies, including coral archives (Woodroffe et al., 2003), lake sediments (Konecky et al., 2016, Fig. 6f; Moy et al., 2002, Fig. 6b), and speleothem records (Hu et al., 2008, Fig. 6d; Zhu et al., 2017, Fig. 6g), document further ENSO intensification, which aligns with the high-variance phase identified in our reconstructions.

This cross-proxy and cross-regional agreement provides robust support for the validity of our findings and underscores the regional coherence of Holocene ENSO dynamics. A key insight from our reconstruction is the pronounced contrast in ENSO behavior between the Mid-Holocene (5829–4200 a BP) and the Late Holocene (4200–2643 a BP). The Mid-Holocene is characterized by generally weak ENSO variability, fewer extreme events, and a persistently La Niña-like background state. In contrast, ENSO variability intensified substantially after ~4200 a BP, with more frequent transitions between El Niño and La Niña, larger SST anomaly amplitudes, and a marked increase in overall ENSO variance, marking a shift toward a more dynamically unstable ENSO regime in the Late Holocene (Fig. 5, Figs. S13–14, Table S5).

5.3. SST–ENSO interactions and climate drivers

5.3.1. La Niña-like phases and SST cooling

Periods of markedly suppressed ENSO variability in our reconstruction are closely associated with prolonged SST cooling in the northern SCS and La Niña-like background states. The weakest ENSO variance occurred during 5814–5794 a BP, representing a 91 % reduction relative to the instrumental baseline of 1994–2023 CE (Table 2). During this interval, mean SST reached its minimum value of ~24.7 °C (Table S4), frequencies of ENSO events were reduced (4.24 El Niño and 3.90 La Niña events per 30 years, Fig. 5d), and interannual SSTA amplitudes were diminished (Fig. 5a,c). Similar, though less extreme, behavior is observed during the long weak-ENSO phase of 4265–3697 a BP, when variance remained on average 59 % below modern levels, frequencies revealed reduced ENSO events (4.06 El Niño events and 3.93 La Niña events per 30 years), and SST exhibited a relatively smooth warming trend with superimposed low-amplitude interannual variability.

Analogous to modern ENSO dynamics, these phases can be explained by a strengthened Walker circulation and enhanced equatorial upwelling, which favor a shallower thermocline in the western Pacific (Cai et al., 2021). In this configuration, relatively cool subsurface waters are more easily ventilated into the upper ocean of the western tropical Pacific and marginal seas such as the SCS, thereby promoting regional SST cooling and suppressing the growth of large ENSO anomalies. The low frequency and amplitude of ENSO events inferred for these intervals are therefore consistent with a dynamically stable, La Niña-biased background state. La Niña-dominated background conditions during comparable periods have been documented in marine sediment and coral records from the western Pacific (Cobb et al., 2013; McGregor et al., 2013).

These La Niña-like periods appear to have been accompanied by distinctive regional hydroclimatic responses. Increased precipitation over the maritime continent likely enhanced riverine discharge into the SCS, as indicated by coeval increases in terrigenous sediment input (Yang et al., 2019) and reductions in salinity. Concurrent weakening of the East Asian summer monsoon (Wang et al., 2005) may have further amplified continental runoff and upper-ocean stratification, thereby reinforcing surface cooling in the northern SCS. This interpretation is supported by synchronous cold anomalies recorded in coral, speleothem, and lacustrine archives across East and Southeast Asia (Asami et al., 2020; Hu et al., 2008; Zhang et al., 2023), suggesting a basin-scale hydroclimatic teleconnection under La Niña-dominated background states.

Table 2
Periods of stronger or weaker ENSO variability (referenced to a variance of 0.0233) on interdecadal scales during 5829–2643 a BP.

Distribution period ±2σ (a BP)	Period duration (year)	Mean ENSO Variance	Mean relative ENSO Variance (%)	Min Variance (%)	Max Variance (%)
5814–5794	21	0.0022	−91	−94	−85
5718–5691	28	0.0426	83	1	124
5690–5242	449	0.0108	−54	−93	2
5241–5214	28	0.0297	27	5	46
5213–5169	45	0.0128	−45	−79	−1
5168–5163	6	0.0242	4	1	6
4652–4588	65	0.0535	129	7	232
4587–4583	5	0.0206	−12	−40	−1
4582–4532	51	0.0686	194	5	372
4531–4484	48	0.0132	−43	−64	−20
4388–4365	24	0.0794	240	3	361
4364–4328	37	0.0181	−23	−43	−2
4327–4314	14	0.0251	8	0	14
4313–4290	24	0.0210	−10	−23	1
4289–4266	24	0.0252	8	0	24
4265–3697	569	0.0096	−59	−91	−1
3696–3563	134	0.0606	160	1	431
3562–3498	65	0.0109	−53	−80	−2
3497–3462	36	0.0346	48	0	84
3461–3416	46	0.0154	−34	−57	−1
3415–3412	4	0.0249	7	5	9
3411–3332	80	0.0147	−37	−62	−1
3331–3279	53	0.041	76	17	157
3278–3253	26	0.0203	−13	−22	0
3252–3226	27	0.0307	32	3	44
2993–2992	2	0.0371	59	57	61
2991–2969	23	0.0188	−19	−45	−1
2968–2953	16	0.0437	87	1	318
2730–2692	44	0.0172	−26	−50	−2
2691–2664	28	0.0272	17	2	26
2663–2657	7	0.0167	−28	−46	−2

5.3.2. *El Niño-like phases and SST warming*

Conversely, periods of intensified ENSO variability are associated with pronounced SST warming and more El Niño-like background conditions in the northern SCS. For example, during 4652–4588 a BP and 3696–3563 a BP (Table 2), anomalously warm SST conditions were identified in our coral records (Table S3), such as 4662–4640 a BP and 3583–3552 a BP. These periods are characterized by frequent El Niño events and greatly elevated ENSO variance. Both the ENSO event structure (Fig. S12b) and the dominant El Niño-like background state (Fig. S13) reflect this regime shift. Mechanistically, under persistently El Niño-like conditions, weakened trade winds and a reduced zonal SST gradient suppress equatorial upwelling and deepen the thermocline in the western tropical Pacific (Cai et al., 2021). Such a configuration reduces vertical mixing and tends to trap heat in the upper ocean of the western Pacific and marginal seas, leading to warmer SSTs and larger interannual anomalies. The large-amplitude ENSO cycles and elevated variance observed in the fossil record therefore reflect a dynamically unstable state of the ENSO system, in which frequent transitions between El Niño-like and La Niña-like conditions occur against a warm background.

These coupled patterns of intensified ENSO variability and regional SST warming are evident in other datasets from the northern SCS (Xu et al., 2017), indicating that prolonged El Niño-like conditions exert significant stress on regional climate and marine ecosystems. Strong interannual SST variability around 3600 a BP has been documented from Line Islands corals (Cobb et al., 2013), and disrupted reef accretion in Panama has been attributed to heightened ENSO variability during that interval (Toth and Aronson, 2019; Toth et al., 2015). Notably, coral bleaching events dated to ~4568 a BP and ~ 3900 a BP (Wang et al., 2021) coincide with intervals of sustained warming and strengthened ENSO variability identified in our reconstruction. This synchronicity suggests that ENSO-driven thermal stress played an important role in triggering bleaching during the Holocene, paralleling the mechanisms responsible for modern warming-induced coral degradation.

5.3.3. *Internally driven ENSO variability*

Our reconstruction suggests a strong correspondence between ENSO state and SST variability throughout the Mid- to Late Holocene. Cooler SSTs tended to occur during La Niña-like phases, whereas warmer conditions coincided with El Niño-like phases, implying a close linkage between ENSO dynamics and regional ocean temperatures in the northern SCS. However, only limited evidence supports external forcings as a major driver of long-term ENSO variability during the Mid- to Late Holocene. Neither reconstructed solar irradiance (Steinhilber et al., 2009, Fig. 6h) nor volcanic activity (Kobashi et al., 2017, Fig. 6i) shows a consistent correspondence with ENSO variance peaks or state transitions in our record. For instance, intervals of elevated ENSO variability (such as 4650–4580 a BP, 4580–4530 a BP, and 3700–3560 a BP) were not accompanied by marked declines in solar irradiance. Likewise, strengthened ENSO variance around 3700–3600 a BP did not coincide with enhanced volcanic forcing; rather, volcanic intensification around 3600–3500 a BP occurred during a period of reduced ENSO variability, suggesting a decoupling of these processes. Taken together, these patterns suggest that external forcings exerted only a limited influence on the long-term modulation of ENSO dynamics during the Mid- to Late Holocene.

Coral $\delta^{18}O$ records from Christmas and Fanning Islands indicate that orbital-scale insolation exerted only limited influence on ENSO dynamics, showing minimal sensitivity since ~7000 a BP (Cobb et al., 2013). Likewise, no statistically significant relationship has been identified between reconstructed ENSO variability and orbital forcing (Emile-Geay et al., 2016), and the impacts of even large volcanic eruptions appear weak and transient in coral $\delta^{18}O$ (Dee et al., 2020). Multiple studies also indicate that ENSO can undergo substantial fluctuations in the absence of clear external triggers (Cobb et al., 2003; Hereid et al., 2013; Zhu et al., 2022). Furthermore, the nonlinear and irregular nature of ENSO variability requires internal ocean–atmosphere processes to be considered in order to explain its Holocene evolution (McGregor and Gagan, 2004).

Taken together, coral-based records, supported by climate model results and other proxy reconstructions, suggest that internal climate dynamics were the primary driver of ENSO variability during the Mid- to Late Holocene. The irregular and oscillatory behavior of ENSO during this period was likely governed by ocean–atmosphere coupling and stochastic processes. Coral growth rate therefore represents a robust dual proxy, capable of recording both SST variations and ENSO-related interannual changes at annual resolution. The 2203-year fossil coral record from the northern SCS reveals complex climate behavior, including tightly linked SST–ENSO fluctuations, and highlights the predominant role of internal processes in modulating ENSO over the past ~6000 years.

6. Conclusion

This study establishes a 2203-year, high-resolution reconstruction of SST and ENSO variability derived from coral growth rates in the northern SCS during the Mid- to Late Holocene. Coral growth rate is demonstrated to be a reliable dual proxy for SST and ENSO variability, effectively capturing the amplitude and frequency of interannual climate fluctuations. The reconstructed annual SST record has a mean of 25.6 ± 0.4 °C (1σ), approximately 0.7 °C lower than the modern baseline (26.3 ± 0.4 °C, 1982–2023 CE). Over this interval, the coral-based SST series reveals at least 14 warm periods and 18 cold periods, with the latter recurring quasi-periodically at ~200-year intervals and shortening in duration toward the Late Holocene. Meanwhile, the reconstructed ENSO variability exhibits multiscale fluctuations, shifting from weaker-than-present, La Niña-like conditions (~5800–4200 a BP) to

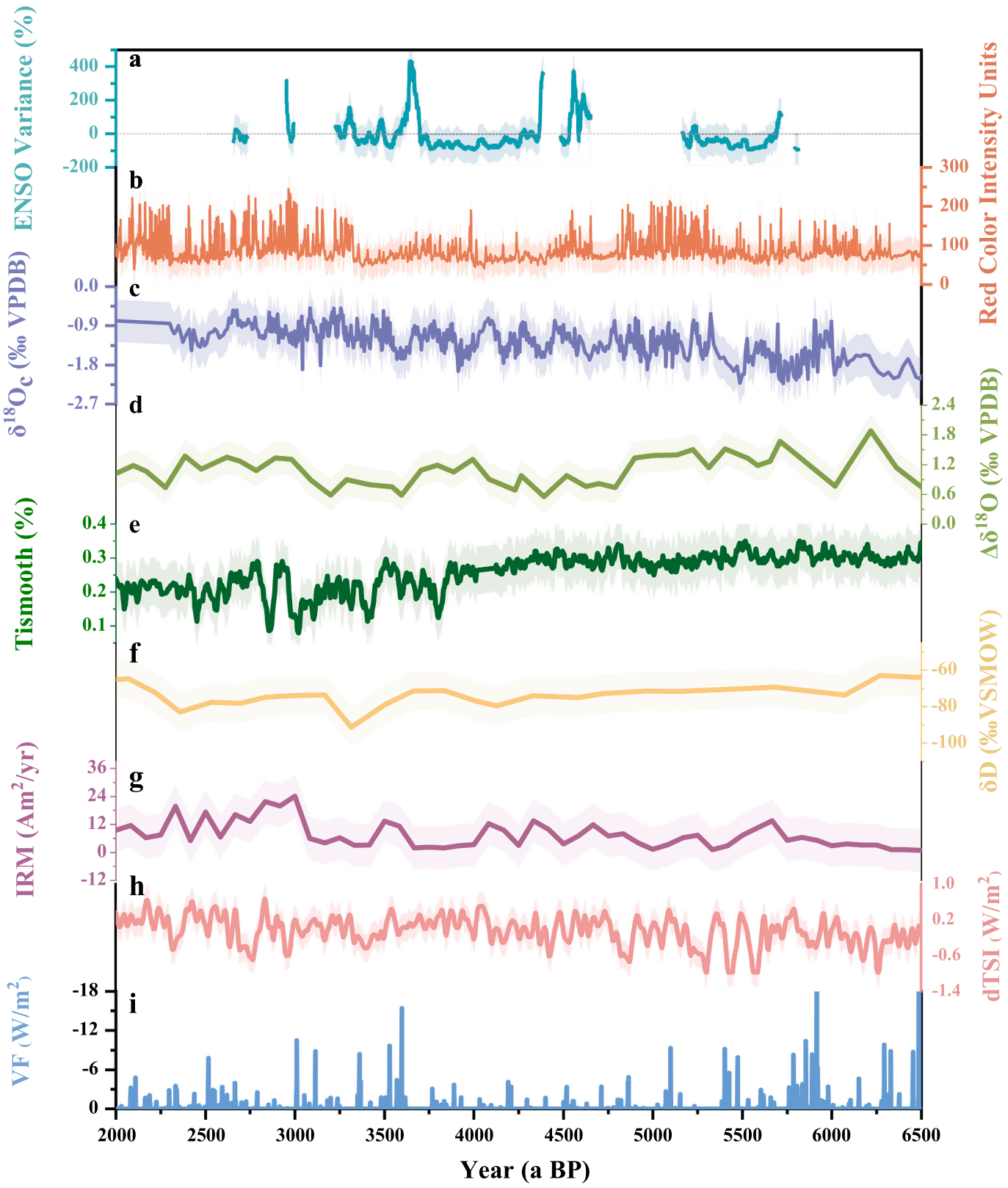

Fig. 6. Reconstructed El Niño–Southern Oscillation (ENSO) variability during the Mid- to Late Holocene compared with regional proxy records and external forcing datasets. (a) Relative ENSO variance derived from a 30-year sliding window (this study). (b) Red colour intensity from Laguna Pallcacocha sediments, southern Ecuador (Moy et al., 2002). (c) ENSO variability inferred from $\delta^{18}O$ records of Qunf Cave (Tian et al., 2023). (d) $\delta^{18}O$ differences between stalagmites from Heshang Cave and Dongge Cave (Hu et al., 2008). (e) Titanium concentrations in Cariaco Basin sediments off the Venezuelan coast (Haug et al., 2001). (f) Leaf-wax hydrogen isotope (δD) variations from Lake Towuti sediments in the Indo-Pacific Warm Pool (Konecky et al., 2016). (g) ENSO intensity reconstruction based on IRM magnetic minerals from a stalagmite in central China (Zhu et al., 2017). (h) Total solar irradiance reconstruction based on ice-core ^{10}Be records (Steinhilber et al., 2009). (i) Volcanic forcing reconstruction from the GISP2 ice core (Kobashi et al., 2017). (For interpretation of the references to colour in this figure legend, the reader is referred to the web version of this article.)

stronger-than-present, El Niño-like conditions (~4200–2600 a BP). Notably, La Niña-like intervals generally coincided with cooler SSTs, whereas El Niño-like phases corresponded to periods of SST warming, indicating strong SST–ENSO coupling. These patterns indicate that long-term ENSO variability cannot be attributed solely to external forcings, such as solar irradiance or volcanic eruptions. Instead, our findings highlight the dominant role of internal climate dynamics, particularly ocean–atmosphere interactions, in driving the nonlinear evolution of ENSO variability during the Mid- to Late Holocene.

CRediT authorship contribution statement

Dahua Huang: Writing – original draft, Software, Methodology, Investigation, Formal analysis. **Kefu Yu:** Writing – review & editing, Supervision, Resources, Project administration, Methodology, Funding acquisition, Conceptualization. **Leilei Jiang:** Writing – review & editing, Software, Formal analysis. **Wei Jiang:** Investigation.

Declaration of competing interest

The authors declare that they have no known competing financial interests or personal relationships that could have appeared to influence the work reported in this paper.

Acknowledgments

This work was funded by the National Natural Science Foundation of China (No. 42030502), Guangxi Scientific Project (No. AD25069075), and the National Key Research and Development Program of China (No. 2023YFF0804801).

Appendix A. Supplementary data

Supplementary data to this article can be found online at https://doi.org/10.1016/j.gloplacha.2025.105259.

Data availability

Supporting data for this study are available in the Zenodo data repository, doi: doi:https://doi.org/10.5281/zenodo.17853637.

References

Abram, N.J., McGregor, H.V., Gagan, M.K., et al., 2009. Oscillations in the Southern Extent of the Indo-Pacific warm Pool during the Mid-Holocene. Quat. Sci. Rev. 28 (25–26), 2794–2803. https://doi.org/10.1016/j.quascirev.2009.07.006.

Adams, J., Mann, M., Ammann, C., 2003. Proxy evidence for an El Niño-like response to volcanic forcing. Nature 426, 274–278. https://doi.org/10.1038/nature02101.

Asami, R., Yoshimura, N., Toriyabe, H., et al., 2020. High-resolution evidence for middle Holocene east Asian winter and summer monsoon variations: snapshots of fossil coral records. Geophys. Res. Lett. 47, e2020GL088509. https://doi.org/10.1029/2020GL088509.

Beck, J., Récy, J., Taylor, F., et al., 1997. Abrupt changes in early Holocene tropical sea surface temperature derived from coral records. Nature 385, 705–707. https://doi.org/10.1038/385705a0.

Bova, S., Rosenthal, Y., Liu, Z., et al., 2021. Seasonal origin of the thermal maxima at the Holocene and the last interglacial. Nature 589, 548–553. https://doi.org/10.1038/s41586-020-03155-x.

Brachert, T.C., Reuter, M., Krüger, S., et al., 2016. Low Florida coral calcification rates in the Plio-Pleistocene. Biogeosciences 13 (15), 4513–4532. https://doi.org/10.5194/bg-13-4513-2016.

Cai, W.J., Borlace, S., Lengaigne, M., et al., 2014. Increasing frequency of extreme El Niño events due to greenhouse warming. Nat. Clim. Chang. 4 (2), 111–116. https://doi.org/10.1038/nclimate2100.

Cai, W.J., McPhaden, M.J., Grimm, A.M., et al., 2020. Climate impacts of the El Niño-Southern Oscillation on South America. Nat. Rev. Earth Environ. 1, 215–231. https://doi.org/10.1038/s43017-020-0040-3.

Cai, W.J., Santoso, A., Collins, M., et al., 2021. Changing El Niño–Southern Oscillation in a warming climate. Nat. Rev. Earth Environ. 2, 628–644. https://doi.org/10.1038/s43017-021-00199-z.

Chen, X.F., Deng, W.F., Xiao, H.F., et al., 2023. Coral paleoclimate perspectives support the role of low-latitude forcing on the 4.2 ka BP event. Geophys. Res. Lett. 50, e2023GL104010. https://doi.org/10.1029/2023GL104010.

Chen, X.F., Deng, W.F., Zhao, J.X., et al., 2024. Interhemispheric synchrony of Mid–Late Holocene SST in the Indo-Pacific warm pool linked to upper water column dynamics. Quat. Sci. Rev. 346, 109064. https://doi.org/10.1016/j.quascirev.2024.109064.

Cobb, K.M., Charles, C., Cheng, H., et al., 2003. El Niño Southern Oscillation and tropical Pacific climate during the last millennium. Nature 424, 271–276. https://doi.org/10.1038/nature01779.

Cobb, K.M., Westphal, N., Sayani, H.R., et al., 2013. Highly variable El Niño-Southern Oscillation throughout the Holocene. Science 339 (6115), 67–70. https://doi.org/10.1126/science.1228246.

Collins, M., An, S.-I., Cai, W., et al., 2010. The impact of global warming on the tropical Pacific Ocean and El Niño. Nat. Geosci. 3 (6), 391–397. https://doi.org/10.1038/ngeo868.

Comboul, M., Emile-Geay, J., Hakim, G.J., et al., 2015. Paleoclimate sampling as a sensor placement problem. J. Clim. 28 (19), 7717–7740. https://doi.org/10.1175/JCLI-D-14-00802.1.

Cooper, T.F., De'Ath, G., Fabricius, K.E., et al., 2008. Declining coral calcification in massive *Porites* in two nearshore regions of the northern Great Barrier Reef. Glob. Chang. Biol. 14 (3), 529–538. https://doi.org/10.1111/j.1365-2486.2007.01520.x.

Cooper, T.F., O'Leary, R.A., Lough, J.M., 2012. Growth of western Australian corals in the Anthropocene. Science 335 (6068), 593–596. https://doi.org/10.1126/science.1214570.

Corrége, T., Delcroix, T., Recy, J., et al., 2000. Evidence for stronger El Niño-Southern Oscillation (ENSO) events in a Mid-Holocene massive coral. Paleoceanography 15, 465–470. https://doi.org/10.1029/1999PA000409.

Dang, S.H., Yu, K.F., Tao, S.C., et al., 2020. El Niño/Southern oscillation during the 4.2 ka event recorded by growth rates of corals from the North South China Sea. Acta Oceanol. Sin. 39 (1), 110–117. https://doi.org/10.1007/s13131-019-1520-5.

Dang, S.H., Liu, Z.F., Yu, K.F., et al., 2024. Reduced ENSO variability during the onset of the 4.2 ka event. Paleoceanogr. Paleoclimatol. 39, e2024PA004923. https://doi.org/10.1029/2024PA004923.

Dee, S.G., Cobb, K.M., Emile-Geay, J., et al., 2020. No consistent ENSO response to volcanic forcing over the last millennium. Science 367, 1477–1481. https://doi.org/10.1126/science.aax2000.

DeLong, K.L., Quinn, T.M., Taylor, F.W., et al., 2013. Improving coral-base paleoclimate reconstructions by replicating 350 years of coral Sr/Ca variations. Palaeogeogr. Palaeoclimatol. Palaeoecol. 373, 6–24. https://doi.org/10.1016/j.palaeo.2012.08.019.

Deser, C., Phillips, A.S., Bourdette, V., et al., 2010. Uncertainty in climate change projections: the role of internal variability. Clim. Dyn. 38 (3–4), 527–546. https://doi.org/10.1007/s00382-010-0977-x.

Emile-Geay, J., Cobb, K.M., Carré, M., et al., 2016. Links between tropical Pacific seasonal, interannual and orbital variability during the Holocene. Nat. Geosci. 9 (2), 168–173. https://doi.org/10.1038/ngeo2608.

Fedorov, A.V., Hu, S., Wittenberg, A.T., et al., 2020. ENSO low-frequency modulation and mean state interactions, El Niño Southern Oscillation in a changing climate. Geophys. Monogr. Ser. 173–198. https://doi.org/10.1002/9781119548164.ch8.

Geng, T., Jia, F., Cai, W.J., et al., 2023. Increased occurrences of consecutive La Niña events under global warming. Nature 619, 774–781. https://doi.org/10.1038/s41586-023-06236-9.

Grothe, P.R., Cobb, K.M., Liguori, G., et al., 2019. Enhanced El Niño-Southern Oscillation variability in recent decades. Geophys. Res. Lett. 47, 7. https://doi.org/10.1029/2019GL083906.

Haug, G.H., Hughen, K.A., Peterson, L.C., et al., 2001. Southward migration of the intertropical convergence zone through the Holocene. Science 293, 1304–1308. https://doi.org/10.1126/science.1059725.

Helmle, K.P., Dodge, R.E., Swart, P.K., et al., 2011. Growth rates of Florida corals from 1937 to 1996 and their response to climate change. Nat. Commun. 2, 215. https://doi.org/10.1038/ncomms1222.

Hereid, K.A., Quinn, T.M., Okumura, Y.M., 2013. Assessing spatial variability in El Niño-Southern Oscillation event detection skill using coral geochemistry. Paleoceanography 28 (1), 14–23. https://doi.org/10.1029/2012PA002352.

Hu, C.Y., Henderson, G.M., Huang, J.H., et al., 2008. Quantification of Holocene Asian monsoon rainfall from spatially separated cave records. Earth Planet. Sci. Lett. 266, 221–232. https://doi.org/10.1016/j.epsl.2007.10.015.

Jiang, L.L., Yu, K.F., Tao, S.C., et al., 2021a. ENSO variability during the medieval climate Anomaly as recorded by *Porites* corals from the northern South China Sea. Paleoceanography and Paleoclimatology 36, e2020PA004173. https://doi.org/10.1029/2020PA004173.

Jiang, L.L., Yu, K.F., Tao, S.C., et al., 2021b. Coral perspective on temperature seasonality and interannual variability in the northern South China Sea during the Roman warm period. Glob. Planet. Chang. 207, 103675. https://doi.org/10.1016/j.gloplacha.2021.103675.

Jiang, L.L., Yu, K.F., Tao, S.C., et al., 2023. Abrupt increase in ENSO variability at 700 CE triggered by solar activity. J. Geophys. Res. Oceans 128, e2022JC019278. https://doi.org/10.1029/2022JC019278.

Jiménez-Moreno, G., Anderson, R.S., Shinker, J.J., 2021. ENSO, sun and megadroughts in SW USA during the last 11,000 years. Earth Planet. Sci. Lett. 576, 117217. https://doi.org/10.1016/j.epsl.2021.117217.

Keefer, D.K., DeFrance, S.D., Moseley, M.E., et al., 1998. Early maritime economy and El Niño events at Quebrada Tacahuay, Peru. Science 281 (5384), 1833–1835. https://doi.org/10.1126/science.281.5384.1833.

Klein, S.A., Soden, B.J., Lau, N.C., 1999. Remote Sea surface temperature variations during ENSO: evidence for a tropical atmospheric bridge. J. Clim. 12 (4), 917–932. https://doi.org/10.1175/1520-0442(1999)012<0917:RSSTVD>2.0.CO;2.

Kobashi, T., Menviel, L., Jeltsch-Thömmes, A., et al., 2017. Volcanic influence on centennial to millennial Holocene Greenland temperature change. Sci. Rep. 7, 1441. https://doi.org/10.1038/s41598-017-01451-7.

Konecky, B., Russell, J., Bijaksana, S., 2016. Glacial aridity in Central Indonesia coeval with intensified monsoon circulation. Earth Planet. Sci. Lett. 437, 15–24. https://doi.org/10.1016/j.epsl.2015.12.037.

Kwiatkowski, L., Cox, P.M., Economou, T., et al., 2013. Caribbean coral growth influenced by anthropogenic aerosol emissions. Nat. Geosci. 6 (5), 362–366. https://doi.org/10.1038/ngeo1780.

Lawman, A.E., Partin, J.W., Dee, S.G., et al., 2020. Developing a coral proxy system model to compare coral and climate model estimates of changes in paleo-ENSO variability. Paleoceanography and Paleoclimatology 35 (7), e2019PA003836. https://doi.org/10.1029/2019PA003836.

Lawman, A.E., Di Nezio, P.N., Partin, J.W., et al., 2022. Unraveling forced responses of extreme El Niño variability over the Holocene. Sci. Adv. 8 (9), eabm4313. https://doi.org/10.1126/sciadv.abm4313.

Lazareth, C.E., Rosell, M.G.B., Turcq, B., et al., 2013. Mid-Holocene climate in New Caledonia (Southwest Pacific): Coral and PMIP models monthly resolved results. Quat. Sci. Rev. 69, 83–97. https://doi.org/10.1016/j.quascirev.2013.02.024.

Lee, H.T., Gruber, A., Ellingson, R.G., et al., 2007. Development of the HIRS outgoing longwave radiation climate dataset. J. Atmos. Ocean. Technol. 24 (12), 2029–2047. https://doi.org/10.1175/2007JTECHA989.1.

Leonard, N.D., Welsh, K.J., Lough, J.M., et al., 2016. Evidence of reduced Mid-Holocene ENSO variance on the Great Barrier Reef, Australia. Paleoceanography 31, 1248–1260. https://doi.org/10.1002/2016PA002967.

Liu, Z.F., Zhao, Y.L., Colin, C., et al., 2016. Source-to-sink transport processes of fluvial sediments in the South China Sea. Earth Sci. Rev. 153, 238–273. https://doi.org/10.1016/j.earscirev.2015.08.005.

Lough, J.M., Barnes, D.J., 1997. Several centuries of variation in skeletal extension, density and calcification in massive *Porites* colonies from the Great Barrier Reef: a proxy for seawater temperature and a background of variability against which to identify unnatural change. J. Exp. Mar. Biol. Ecol. 211 (1), 29–67. https://doi.org/10.1016/S0022-0981(96)02710-4.

Lough, J.M., Barnes, D.J., 2000. Environmental controls on growth of the massive coral *Porites*. J. Exp. Mar. Biol. Ecol. 245 (2), 225–243. https://doi.org/10.1016/S0022-0981(99)00168-9.

Marcott, S.A., Shakun, J.D., Clark, P.U., et al., 2013. A reconstruction of regional and global temperature for the past 11,300 years. Science 339 (6124), 1198–1201. https://doi.org/10.1126/science.1228026.

McGregor, H.V., Gagan, M.K., 2004. Western Pacific coral $\delta^{18}O$ records of anomalous Holocene variability in the El Niño-Southern Oscillation. Geophys. Res. Lett. 31, L11204. https://doi.org/10.1029/2004GL019972.

McGregor, H.V., Fischer, M.J., Gagan, M.K., et al., 2013. A weak El Niño/Southern Oscillation with delayed seasonal growth around 4,300 years ago. Nat. Geosci. 6 (11), 949–953. https://doi.org/10.1038/ngeo1936.

McPhaden, M.J., 2015. Playing hide and seek with El Niño. Nat. Clim. Chang. 5, 791–795. https://doi.org/10.1038/nclimate2775.

McPhaden, M.J., Zebiak, S.E., Glantz, M.H., 2006. ENSO as an integrating concept in earth science. Science 314 (5806), 1740–1745. https://doi.org/10.1126/science.1132588.

Moy, C.M., Seltzer, G.O., Rodbell, D.T., et al., 2002. Variability of El Niño/Southern Oscillation activity at millennial timescales during the Holocene epoch. Nature 460, 162–165. https://doi.org/10.1038/nature01194.

Nie, B.F., Chen, T.G., Liang, M.T., et al., 1997. Relationship between coral growth rate and sea surface temperature in the northern part of South China Sea during the past 100 a. Sci. China Ser. D Earth Sci. 40 (2), 173–182. https://doi.org/10.1007/BF02878376.

Rein, B., Lückge, A., Reinhardt, L., et al., 2005. El Niño variability off Peru during the last 20,000 years. Paleoceanography 20, PA4003. https://doi.org/10.1029/2004PA001099.

Reuter, M., Brachert, T.C., Kroeger, K.F., 2005. Diagenesis of growth bands in fossil Scleractinia corals: identification and modes of preservation. Facies 51 (1–4), 146–159. https://doi.org/10.1007/s10347-005-0064-7.

Rodriguez, L.G., Cohen, A.L., Ramirez, W., et al., 2019. Mid-Holocene, coral-based sea surface temperatures in the western tropical Atlantic. Paleoceanography and Paleoclimatology 34 (7), 1234–1245. https://doi.org/10.1029/2019PA003571.

Sadler, J., Webb, G.E., Leonard, N.D., et al., 2016. Reef core insights into Mid-Holocene water temperatures of the southern Great Barrier Reef. Paleoceanography 31 (10), 1395–1408. https://doi.org/10.1002/2016PA002943.

Saenger, C., Cohen, A.L., Oppo, D.W., et al., 2009. Surface-temperature trends and variability in the low-latitude North Atlantic since 1552. Nat. Geosci. 2 (7), 492–495. https://doi.org/10.1038/ngeo552.

Solow, A.R., Huppert, A., 2004. A potential bias in coral reconstruction of sea surface temperature. Geophys. Res. Lett. 31 (6), L06308. https://doi.org/10.1029/2003GL019349.

Steinhilber, F., Beer, J., Fröhlich, C., 2009. Total solar irradiance during the Holocene. Geophys. Res. Lett. 36 (19), L19704. https://doi.org/10.1029/2009GL040142.

Stott, L., Cannariato, K., Thunell, R., et al., 2004. Decline of surface temperature and salinity in the western tropical Pacific Ocean in the Holocene epoch. Nature 431, 56–59. https://doi.org/10.1038/nature02903.

Sun, D.H., Gagan, M.K., Cheng, H., et al., 2005. Seasonal and interannual variability of the Mid-Holocene East Asian monsoon in coral $\delta^{18}O$ records from the South China Sea. Earth Planet. Sci. Lett. 237 (43467), 69–84. https://doi.org/10.1016/j.epsl.2005.06.022.

Tan, W., Wang, X., Wang, W.Q., et al., 2016. Different responses of sea surface temperature in the South China Sea to various El Niño events during boreal autumn. J. Clim. 29, 1127–1142. https://doi.org/10.1175/JCLI-D-15-0338.1.

Tao, S.C., Liu, Kam-biu, Yan, H.Q., et al., 2024. SST and ENSO activity 282,000 years ago reconstructed from *Porites* coral in the South China Sea. Glob. Planet. Chang. 237, 104455. https://doi.org/10.1016/j.gloplacha.2024.104455.

Tian, Y., Fleitmann, D., Zhang, Q., et al., 2023. Holocene climate change in southern Oman deciphered by speleothem records and climate model simulations. Nat. Commun. 14, 4718. https://doi.org/10.1038/s41467-023-40454-z.

Timmermann, A., An, S.-I., Kug, J.-S., et al., 2018. El Niño–Southern Oscillation complexity. Nature 559 (7715), 535–545. https://doi.org/10.1038/s41586-018-0252-6.

Toth, L.T., Aronson, R.B., 2019. The 4.2ka event, ENSO, and coral reef development. Clim. Past 15, 105–119. https://doi.org/10.5194/cp-15-105-2019.

Toth, L.T., Aronson, R.B., Cobb, K.M., et al., 2015. Climatic and biotic thresholds of coral-reef shutdown. Nat. Clim. Chang. 5, 369–374. https://doi.org/10.1038/nclimate2541.

Tudhope, A.W., Chilcott, C.P., Mcculloch, M.T., et al., 2001. Variability in the El Niño–Southern Oscillation through a Glacial-Interglacial cycle. Science 291 (5508), 1511–1517. https://doi.org/10.1126/science.1057969.

Vialard, J., Jin, F.-F., McPhaden, M.J., et al., 2025. The El Niño Southern Oscillation (ENSO) recharge oscillator conceptual model: achievements and future prospects. Rev. Geophys. 63, e2024RG000843. https://doi.org/10.1029/2024RG000843.

Wang, B., Wu, R.G., Fu, X.H., 2000. Pacific-East Asian teleconnection: how does ENSO affect East Asian climate? J. Clim. 13 (9), 1517–1536. https://doi.org/10.1175/1520-0442(2000)013<1517:PEATHD>2.0.CO;2.

Wang, Y.J., Cheng, H., Edwards, R.L., et al., 2005. The Holocene Asian Monsoon: Links to solar changes and North Atlantic climate. Science 308 (5723), 587–854. https://doi.org/10.1126/science.1106296.

Wang, H., Yu, K.F., Tao, S.C., et al., 2021. New evidence for the periodic bleaching and recovery of *Porites* corals during the Mid–Late Holocene in the northern South China Sea. Glob. Planet. Chang. 197, 103397. https://doi.org/10.1016/j.gloplacha.2020.103397.

Wang, F., Li, X.G., Tang, X.H., et al., 2023. The seas around China in a warming climate. Nat. Rev. Earth Environ. 4, 535–551. https://doi.org/10.1038/s43017-023-00453-6.

Wittenberg, A.T., 2009. Are historical records sufficient to constrain ENSO simulations? Geophys. Res. Lett. 36 (12). https://doi.org/10.1029/2009GL038710.

Woodroffe, C.D., Beech, M.R., Gagan, M.K., 2003. Mid–Late Holocene El Niño variability in the equatorial Pacific from coral microatolls. Geophys. Res. Lett. 30 (7), 1358. https://doi.org/10.1029/2002GL015868.

Xu, S.D., Yu, K.F., Tao, S.C., et al., 2017. Evidence for the thermal bleaching of *Porites* corals from 4.0 ka B.P. In the Northern South China Sea. J. Geophys. Res. Biogeosci. 123, 79–94. https://doi.org/10.1002/2017JG004091.

Yan, H., Sun, L.G., Wang, Y.H., et al., 2011. A record of the Southern Oscillation Index for the past 2,000 years from precipitation proxies. Nat. Geosci. 4 (9), 611–614. https://doi.org/10.1038/ngeo1231.

Yancheva, G., Nowaczyk, N.R., Mingram, J., et al., 2007. Influence of the intertropical convergence zone on the East Asian monsoon. Nature 445 (7123), 74–77. https://doi.org/10.1038/nature05431.

Yang, Y.P., Xiang, R., Liu, J.G., et al., 2019. Inconsistent Sea surface temperature and salinity changing trend in the northern South China Sea since 7.0 ka BP. J. Asian Earth Sci. 171, 178–186. https://doi.org/10.1016/j.jseaes.2018.05.033.

Yu, K.F., 2012. Coral reefs in the South China Sea: their responses to and records on past environmental changes. Sci. China Earth Sci. 55 (8), 1217–1229. https://doi.org/10.1007/s11430-012-4449-5.

Yu, K.F., Zhao, J.X., Wei, G.J., et al., 2005. Mid–Late Holocene monsoon climate retrieved from seasonal Sr/Ca and $\delta^{18}O$ records of *Porites lutea* corals at Leizhou Peninsula, northern coast of South China Sea. Glob. Planet. Chang. 47 (2), 301–316. https://doi.org/10.1016/j.gloplacha.2004.10.018.

Yu, K.F., Zhao, J.X., Shi, Q., et al., 2006. U-series dating of dead *Porites* corals in the South China Sea: evidence for episodic coral mortality over the past two centuries. Quat. Geochronol. 1 (2), 129–141. https://doi.org/10.1016/j.quageo.2006.06.005.

Yu, K.F., Hua, Q., Zhao, J.X., et al., 2010. Holocene marine ^{14}C reservoir age variability: evidence from ^{230}Th-dated corals in the South China Sea. Paleoceanography 25, PA3205. https://doi.org/10.1029/2009PA001831.

Zhang, H.L., Yu, K.F., Shi, Q., et al., 2014. Sea surface temperature variations during the Mid–Late Holocene reconstructed by *Porites* coral growth rates in the Xisha Islands. Quat. Sci. 34 (6), 1296–1305. https://doi.org/10.3969/j.issn.1001-7410.2014.06.19.

Zhang, E.L., Meng, X.Q., Ning, D.L., et al., 2023. Holocene extreme hydroclimate events in the Asian monsoon region were more frequent during cooler intervals. Commun. Earth Environ. 4, 344. https://doi.org/10.1038/s43247-023-00997-x.

Zhao, J.X., Yu, K.F., Feng, Y.X., 2009. High-precision ^{238}U-^{234}U-^{230}Th disequilibrium dating of the recent past: a review. Quat. Geochronol. 4 (5), 423–433. https://doi.org/10.1016/j.quageo.2009.01.012.

Zhou, P.C., Yan, H., Han, T., et al., 2022. Mid to late Holocene ENSO variability reconstructed by high-resolution Tridacna Sr/Ca records from the northern part of the South China Sea. Palaeogeogr. Palaeoclimatol. Palaeoecol. 601, 111117. https://doi.org/10.1016/j.palaeo.2022.111117.

Zhu, Z.M., Feinberg, J.M., Xie, S.C., et al., 2017. Holocene ENSO-related cyclic storms recorded by magnetic minerals in speleothems of Central China. Proc. Natl. Acad. Sci. USA 114 (5), 852–857. https://doi.org/10.1073/pnas.1610930114.

Zhu, F., Emile-Geay, J., Anchukaitis, K.J., et al., 2022. A re-appraisal of the ENSO response to volcanism with paleoclimate data assimilation. Nat. Commun. 13, 747. https://doi.org/10.1038/s41467-022-28210-1.